

Accurate, uncertainty-aware classification of molecular chemical motifs from multi-modal X-ray absorption spectroscopy

Matthew R. Carbone,^{1,*} Phillip M. Maffettone,² Xiaohui Qu,³ Shinjae Yoo,¹ and Deyu Lu^{3,†}

¹*Computational Science Initiative, Brookhaven National Laboratory, Upton, New York 11973, USA*

²*National Synchrotron Light Source II, Brookhaven National Laboratory, Upton, NY 11973, USA*

³*Center for Functional Nanomaterials, Brookhaven National Laboratory, Upton, New York 11973, USA*

(Dated: June 29, 2023)

Accurate classification of molecular chemical motifs from experimental measurement is an important problem in molecular physics, chemistry and biology. In this work, we present neural network ensemble classifiers for predicting the presence (or lack thereof) of 41 different chemical motifs on small molecules from simulated C, N and O K-edge X-ray absorption near-edge structure (XANES) spectra. Our classifiers not only reach a maximum average class-balanced accuracy of 0.99 but also accurately quantify uncertainty. We also show that including multiple XANES modalities improves predictions notably on average, demonstrating a “multi-modal advantage” over any single modality. In addition to structure refinement, our approach can be generalized for broad applications with molecular design pipelines.

Introduction— Artificial intelligence and machine learning (AI/ML), and more broadly data-driven methods, have made a huge impact in our society over the last decade, with exciting applications in image processing, self-driving vehicles and natural language processing using generative AI. The adaptation of AI/ML methods in scientific research has quickly spread to a wide range of domains, from fundamental research in physics [1–6], chemistry [7–9], biology [10] and materials science [11–14] to applications in drug discovery pipelines [15, 16] and autonomous experimentation/self-driving laboratories [17–22].

In the field of atomic scale modeling, of particular interest are AI/ML approaches that allow for insights into the structure-property relationship, which is key to the understanding of the fundamental physics that ultimately leads to practical applications. These can take different forms, such as ML surrogates that predict molecular or materials properties from the atomic structure, thus bypassing expensive quantum mechanics simulations (i.e., the forward problem) [7, 23], ML classifiers that extract physical descriptors from experimental measurements (i.e., the inverse problem) [11, 24], or autoencoders that can interpret the physical meaning of latent space variables [25, 26].

In this study, we will focus on a specific type of the inverse problem, which extracts local structural and chemical information from the near edge features of X-ray absorption spectra, known as X-ray absorption near edge structure (XANES). XANES is a widely used materials characterization technique that is element specific and sensitive to the local chemical environment of the absorbing site (e.g., charge state, coordination number and local symmetry). Recently, significant progress has been made in solving the inverse problem using ML

techniques, including predicting the average coordination numbers of metal nanoparticles [24, 27] and the local chemical environment of materials (e.g., transition metal cations [11, 12, 28] and amorphous carbon [29, 30]). In molecular systems, Carbone *et al.* performed principal component analysis (PCA) of simulated molecular N and O K-edge XANES and showed that the features in the reduced dimension has a strong correlation with the N and O-containing chemical motifs [31]. Tetef *et al.* used various unsupervised methods (including PCA, variational autoencoders, t-distributed stochastic neighbour embedding, and the uniform manifold approximation and projection) on P and S K-edge XANES to quantify the spectral sensitivity on the local chemical environment of organophosphorus and organosulfur compounds [32, 33]. They also showed that valence-to-core X-ray emission spectra can provide similar chemical information in character and content [32]. Despite this recent progress, an accurate and uncertainty-aware XANES-based ML classifier of a broad range of molecular chemical motifs has not yet been reported.

In this letter, we show how uncertainty-aware neural network classifiers can be used to predict 41 different chemical motifs to very high accuracy, using multiple XANES signals as input. These ML classifiers can have important applications in environmental chemistry [34], paleontology [35], organic geochemistry [36], and space science [37]. We also evaluate the effectiveness of the UQ algorithms, and demonstrate a “multi-modal advantage”: the accuracy of the classifiers is significantly higher when using multiple XANES signals from different absorbing elements when compared to using only single modalities independently.

Methods— To construct our dataset, molecular carbon, nitrogen and oxygen K-edge XANES were computed using the multiple scattering code FEFF9 [38]. Density Functional Theory-relaxed molecular structures are sourced from the QM9 database [39], a subset of the GDB-17 chemical universe [40]. Each molecule in

* mcarbone@bnl.gov

† dlu@bnl.gov

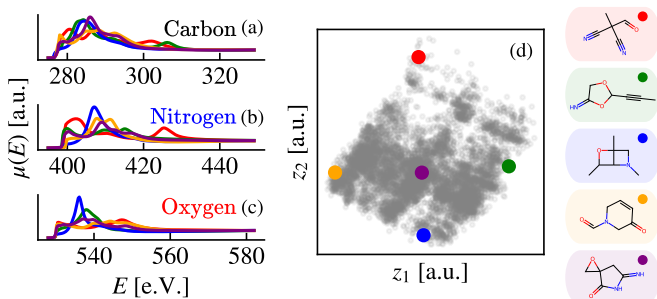


FIG. 1. Five exemplary molecules from the \mathcal{D}_{CNO} database and their corresponding spectra. Carbon, nitrogen and oxygen K-edge XANES are shown (a-c). PCA is used to decompose the full spectral dataset (C, N and O K-edge XANES stitched together). The coefficients of the first two principal axes, z_1 and z_2 , are plotted in (d) as grey background. The location of these example spectra are shown as colored markers. The corresponding molecules are show to the right of (d).

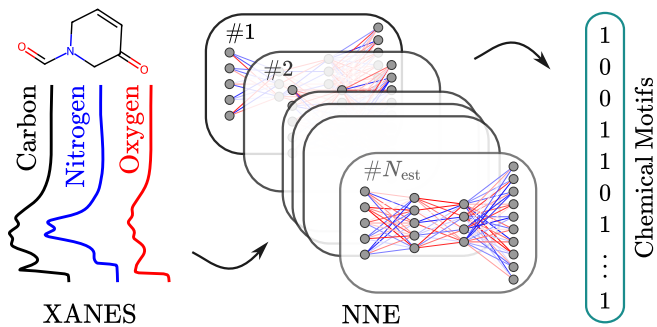


FIG. 2. Multimodal XANES spectra (C, N and O signals) are fed into individual neural networks, which constitute a neural network ensemble (NNE) of E estimators, to predict a binary vector, each entry of which corresponds to the presence (or lack thereof) of a specific chemical motif.

the QM9 dataset ($\approx 134\text{k}$ small molecules) contains at most 9 heavy atoms (C, N, O and F). We partition the QM9 database into non-disjoint subsets based on which atoms are present (and thus which XANES signals exist). For example, \mathcal{D}_{CN} is the subset of QM9 in which every molecule contains *at least* one C and one N atom, and thus at least a C and N XANES signal. We use the same database as in Ghose *et al.* [41], which is available open access [42]. As a preliminary analysis, we perform PCA on the \mathcal{D}_{CNO} dataset and show that spectra of exemplary molecules with different chemical motifs are well separated in the spectral latent space (see Fig. 1).

The trend from the PCA analysis agrees with the studies in the literature that established the spectral fingerprints (in C, O, and N K-edge XANES) of molecular chemical motifs [43]. In C K-edge XANES, distinct lower energy features in alkenyl and aromatic species are assigned to $1s$ to π^* transitions [36, 44] and relative intense near edge features in saturated carbon (e.g., methyl and methylene) are assigned to the transitions of $1s$ to the

$3p/\sigma^*$ hybrid state involving mixing of a $3p$ Rydberg state with a σ^* C-H orbital [45]. Similarly, in N K-edge XANES, the $1s$ to π^* transitions are characteristic of unsaturated N species (e.g., imine and nitrile) as compared to the $1s$ to the $3p/\sigma^*$ excitations in saturated N chemical motifs (e.g., amine and pyrrole) [43]. O K-edge XANES of small molecules can be used to extract ratio of single to double bonded oxygen [43].

As the goal of this work is inferring chemical information from XANES spectra, we choose 41 chemical motifs (see Fig. S3 and Table S1 in the Supplemental Material for their definitions), including many common functional groups, as the target quantity for machine learning. Using SMARTS pattern matching and Open Babel [46], each molecule is assigned a list of the chemical motifs (alcohols, ketones, aromatic character, alkynes, nitriles, etc.) that it contains. For each dataset, only chemical motifs that occur with frequency $\in [0.05, 0.95]$ in the dataset are used for training and evaluation.

The workflow of this work is shown in Fig. 2. The QM9 XANES spectra, $\mu^{(i)}$, are used as inputs to fully connected deep neural networks (DNNs), which are tasked with predicting the presence (or lack thereof) of 41 chemical motifs. Each modality of XANES spectra (C, N and O) is of length 200 on a pointwise grid. The target, $\mathbf{y}^{(i)}$, is a binary vector, where $y_j^{(i)} = 1$ if at least one instance of chemical motif j is present on training example i , and 0 otherwise (in principle, in experimental measurements the number of absorbing atoms can be associated with the edge jump Δ , which would provide an additional constraint in e.g. the inverse problem). The last layer of each DNN is a sigmoid activation function, $\sigma(x) = 1/(1 + e^{-x}) \in (0, 1)$, and a mean squared error loss is used to train the continuous neural network output, $\hat{\mathbf{y}}^{(i)}$, to best predict the binary targets. While this is formally a multi-task, binary *classification* problem, models are trained using a regression approach and produce continuous outputs. Results are then rounded during inference.

For the main results of this work, each dataset is partitioned into a training (72.25%), validation/hyperparameter tuning (12.75%) and testing (15%) split. We perform hyper-parameter tuning using Optuna [47], in which the dropout rate, neural network architecture and initial learning rate are varied. All results in this manuscript are presented on the testing set using the best model as evaluated on the validation set.

To quantify the performance of our models, we utilize the class-balanced accuracy (CBA) scalar metric. The CBA is defined as the mean of the sensitivity and specificity,

$$\text{CBA} = \frac{1}{2} \left[\frac{T_+}{T_+ + F_-} + \frac{T_-}{T_- + F_+} \right],$$

where T_{\pm} (F_{\pm}) are the number of true (false) positives (negatives). In the case of a model taking advantage of a highly imbalanced data (one class dominates in propensity and the model predicts that class almost every time),

the CBA will reduce to 0.5 in the binary classification case (unlike the accuracy, which will be erroneously inflated). This is important for this problem, as some chemical motifs occur with frequency only $\approx 5\%$.

The CBA core obtained from the testing set can be treated as a proxy for how well the ML model will perform on unseen data, like in standard ML surrogate use cases. However, such models are not “uncertainty aware”, i.e., they do not produce a measure of confidence on any given training example. As ML methods are inherently interpolative procedures [48], knowing when data drifts out-of-sample is of key importance. Uncertainty quantification (UQ) is a set of statistical methods broadly classified as predictive methods for accurately estimating statistical uncertainty. UQ as applied to ML includes a measure of model confidence in addition to the model output. In this work, we apply neural network ensembles (NNEs, in similar fashion to previous research by the authors [41]) to quantify the uncertainty in the model predictions. Twenty individual estimators are generated by a combination of training set down-sampling and architecture randomization. Starting from the scaffold of the best performing architecture from the previous hyper-parameter search, the number of neurons in each layer is randomly changed by adding or subtracting a small integer. In addition, a different random subset of the training set (5%) is removed for each estimator in the ensemble. These two methods together create sufficient model diversity to leverage the “wisdom of the crowd” principle [49]: the estimate of the aggregated opinion of a diverse set of estimators is more robust than any single estimator. Such NNEs are generally a more sensible option than any single estimator for production applications.

Results/Discussion— We first evaluate the CBA performance of single- and multi-modality models on the testing set. Using \mathcal{D}_{CNO} , we execute the previously described pipeline (training, Optuna-powered hyper-parameter tuning, and evaluation on the testing set) on only certain subsets of the feature space. For example, we define $\mathcal{D}_{\text{CNO}}^{[\text{C}]}$ as the same dataset as \mathcal{D}_{CNO} (including the same train/validation/testing splits) but only using the C XANES as input. For each $\{\mathcal{D}_{\text{CNO}}^{[\text{C}]}, \mathcal{D}_{\text{CNO}}^{[\text{N}]}, \mathcal{D}_{\text{CNO}}^{[\text{O}]}, \mathcal{D}_{\text{CNO}}\}$, an optimal model is found via hyper-parameter tuning, and the results of the best model evaluated on the testing set. These results are shown in Fig. 3.

Including additional modalities usually improves model performance (as graded by CBA), and at worst simply does not improve over single modalities. For example, nitriles and amides have distinct fingerprints in both the C and N K-edge XANES, and similarly alcohols and carboxyl groups do in C and O K-edge XANES. We highlight that these results are obtained independently from pure data analysis approach without domain knowledge, and they reproduce the known correlation in the literature [43]. These signals are all that are necessary

to perform accurate classification and thus including extra modalities does not substantially improve CBA. On the other hand, 1,2-aminoalcohols are more complex motifs (containing multiple absorbing atom types, multiple types of chemical bonds, etc.) that are harder to resolve without inputs from all three modalities, and thus result in roughly a 5% CBA gain over the highest-performing single modality.

The complementary information from the combination of multimodal XANES measurements can be understood using a tight-binding picture. For a qualitative discussion, we ignore many-body physics and map the atomic structure of a small molecule to a tight-binding Hamiltonian that contains on-site orbital energies and hopping integrals. To further simplify the problem, we take the projected density of states of the unoccupied bands under the quasi-particle picture as a proxy of the K-edge XANES spectra. The peak positions and their intensities of the spectrum correspond to eigenvalues and the weights of p orbitals of the absorbing atoms. Solving the inverse problem with single modality requires one to deduce the matrix elements of the tight-binding Hamiltonian (e.g., on-site energies of atoms other than the absorber and hopping integrals). Multimodal XANES signals supply more complete information of the unoccupied molecular orbitals (i.e., with weights on multiple atom types) and reduce the dimension of the parameter space (i.e., by knowing on-site energies of multiple atom types). As a result, multimodal XANES analysis represents an advantage in solving the inverse problem.

Furthermore, we highlight that *all* CNO models are incredibly accurate, with an average CBA score of 0.99 ± 0.01 across all examined chemical motifs, which is promising for future downstream applications such as targeted molecular refinement [8]. We also find similar results using all combinations of \mathcal{D}_{AB} for $A, B \in \{\text{C}, \text{N}, \text{O}\}$ (which are distinct datasets from \mathcal{D}_{CNO}), with the highest multi-modal advantage as large as 7% in the case of \mathcal{D}_{NO} . Finally, there are certain cases where XANES signals originate from atoms not precisely contained in the given chemical motifs, such as a signal from the N K-edge trying to predict an alcohol. These cases are kept for completeness and shown as open circles in Fig. 3. Cases in which these signals contribute positively to the accuracy of the models are likely due to non-local correlations between different parts of the small molecules, which may worth further investigation.

For future applications such as targeted molecular structure generation via structure search algorithms, it is important that the confidence of model prediction can be quantified. That way, an out-of-sample prediction can be confidently discarded, and confident predictions can be trusted. Towards this end, we perform UQ in similar fashion to Ref. 41, using an ensemble of 20 models built off of the scaffold of the best performing model from the hyper-parameter tuning procedure. To evaluate the performance of the UQ procedure, we analyze the CBA as a function of the “number of deviating estimators”

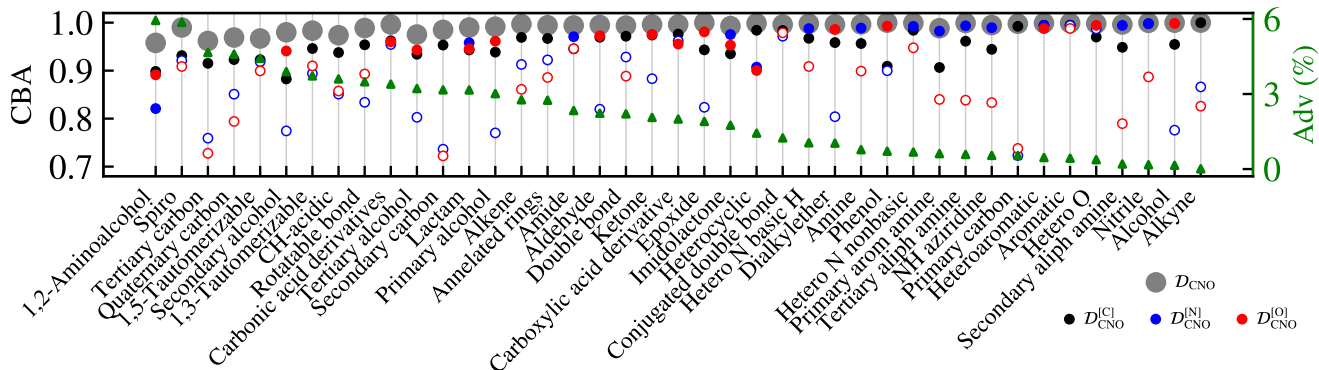


FIG. 3. CBA scores for each model of the three single-modality models and the multi-modal model. Results are resolved by chemical motif and sorted (left to right) by decreasing multi-modal advantage (“Adv”) as evaluated using the CBA metric. This advantage is defined by the difference of the \mathcal{D}_{CNO} result and the best performing single modality result. Open circles represent cases in which the XANES signal originates from an atom not contained in the corresponding chemical motif (e.g. an open blue circle for an alcohol).

(NDE): the number of estimators that deviate from the aggregate. Consider N_{est} total estimators, where $N_{\text{est}} - n$ estimators predict $\hat{y}_j = 0$ (or 1), and $n < N_{\text{est}} - n$ estimators predict 1 (or 0). In this case, n estimators have deviated from the majority opinion, and thus n is the NDE. The NDE can also be regarded as an integral proxy for the spread of the estimator predictions. Regardless, as NDE increases, it is intuitive that CBA will decrease, since more disagreement would imply more uncertainty. Note that when $n = N_{\text{est}}/2$, CBA will always be 1/2 according to its definition (when all estimators disagree, the prediction will be 0.5, which is always rounded to 0). This means that only a single class is predicted, and in this case, CBA is equal to 0.5).

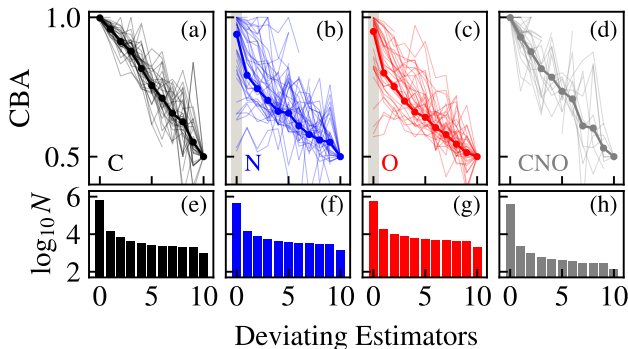


FIG. 4. Uncertainty quantification using neural network ensembles, resolved by chemical motif. (a)-(d) Class-balanced accuracy as a function of the number of deviating estimators, for each chemical motif (thin lines) and averaged across the entire dataset. Data in which there are < 10 examples are discarded from each bin due to lack of sufficient statistics. (e)-(h) The number of total training examples (\times the number of chemical motifs) contained in the full dataset as a function of the number of deviating estimators.

We plot the average testing set CBA results over the

NNEs and chemical motifs in Fig. 4(a)-(d) with the resolved individual chemical motifs shown as thin lines. For all three single modalities as well as the CNO multi-modal result, CBA decreases monotonically with NDE on average. For $\mathcal{D}_{\text{CNO}}^{[\text{C}]}$ and \mathcal{D}_{CNO} , when all estimators are in agreement, the models are essentially perfectly accurate. These cases also constitute the vast majority of the data, as shown in Fig. 4(e)-(h). As soon as a single estimator begins to deviate, the CBA score drops. The effect is even more significant in the $\mathcal{D}_{\text{CNO}}^{[\text{N}]}$ and $\mathcal{D}_{\text{CNO}}^{[\text{O}]}$ cases, where in contrast, the model CBA scores are much lower on average even with 0 deviating estimators. This is due to the chemical nature of chemical motifs in small molecules: almost all contain C as part of their backbone, making it logical that signals from N- and O-containing chemical motifs are embedded in C K-edge XANES. Conversely, there is no reason to expect that in general, N K-edge XANES contains a signature for O-containing chemical motifs (except due to dataset-dependent correlations, such as when N and O are often nearest-neighbors in a dataset). Indeed, almost all chemical motifs in Fig. 4(b) and (c) with CBA less than 0.9 at 0 NDE (corresponding to the indicated grey area) in the $\mathcal{D}_{\text{CNO}}^{[\text{N}]}$ and $\mathcal{D}_{\text{CNO}}^{[\text{O}]}$ results do not contain the absorbing element. While presented here for completeness, one would simply not use these models in real deployment scenarios in which high performance is demanded.

To further examine the advantage of utilizing information from multiple modalities in more realistic situations, we performed a secondary study in a subset of QM9 containing, where molecules with 8 or less heavy atoms were used for training/validation, and molecules with 9 heavy atoms were used for testing (henceforth referred to as the 8/9 split). This split tests two hypothesis: whether or not the multi-modal advantage is still present in a case with severely limited training data, and if these models can generalize to molecules slightly larger than those in the training set. We find that these models are also

performant, with a CBA score of 0.96 ± 0.03 across all chemical motifs, and that the same UQ trends in Fig. 4 are recovered. These results are presented in detail in the Supplemental Material.

Conclusions— We presented uncertainty-quantifying classifiers for predicting 41 different chemical motifs in small molecules from K-edge XANES spectra. Our models not only perform exceptionally well in the classification task, they are also able to accurately quantify uncertainty. Although the QM9 dataset represents a limited chemical space and simulated XANES can have discrepancies with experiment [11], our workflow is entirely general and can in principle be applied to different levels of theory, more complex datasets, and experiment, if a large number of labeled measurements are available. In summary, we demonstrate the usefulness of uncertainty-quantifying models and multi-modal inputs and believe that both of them key to future progress in the field.

Acknowledgements— The authors would like to acknowledge helpful discussions with Mark S. Hybertsen. This material is based upon work supported by the U.S. Department of Energy, Office of Science, Office of Basic Energy Sciences, under Award Numbers FWP PS-030 and DE-SC-0012704. This research used the Theory and Computation resources of the Center for Functional Nanomaterials, which is a U.S. DOE Office of Science Facility, and the Scientific Data and Computing Center at Brookhaven National Laboratory under Contract No. DE-SC0012704.

Software and data availability— All code/data used in this manuscript can be found open source/access at

- github.com/AI-multimodal/multimodal-molecules,
- github.com/matthewcarbone/Crescendo,
- doi.org/10.5281/zenodo.8087823.

Supplemental Material: Accurate, uncertainty-aware classification of molecular chemical motifs from multi-modal X-ray absorption spectroscopy

S1. METHODOLOGICAL DETAILS

We henceforth outline the details of our methodology, starting from the raw data and ending with the training and evaluation procedures.

We begin with the same dataset from Ref. 41, which can be found at doi.org/10.5281/zenodo.7554888. This dataset contains the site-wise XANES spectra for all C, N and O sites in the QM9 database. From there, it is processed into molecular XANES spectra. Any molecule in which at least one XANES spectrum was missing/failed to converge was discarded. This new dataset can be found here: doi.org/10.5281/zenodo.8087823. The following steps, which are also contained in the `scripts` directory in our `multimodal-molecules` GitHub repository (all paths are relative to the root directory of this repository), are as follows.

S1.1. Identification of chemical motifs from SMILES representation

From the file `xanes.pkl`, all SMILES strings are extracted and saved as a text file. Open Babel is then used in conjunction with the FP4 fingerprinting method, corresponding to SMARTS queries stored in the Open Babel GitHub repository github.com/openbabel/openbabel/blob/master/data/SMARTS_InteLigand.txt. Ultimately, this process results in a source of truth file `index.csv`, which contains a binary indicator of which functional groups are present on which molecule. Similarly, `xanes.pkl` is the mapping between SMILES and XANES spectra. These two files are used in constructing the training/validation/testing datasets in the next steps. These steps can be reproduced by running `scripts/00_get_functional_groups.py` and `scripts/01_create_index.py` in succession.

S1.2. Dataset construction

For every possible modality combination (and for the 8/9 dataset split), we create training/validation/testing splits. The data are saved in a format readable by our "easy execution" machine learning code, Crescendo, which leverages Lightning and Hydra for easily trainable models and neural network ensembles. This format essentially requires a directory with NumPy binary files like `X_train.npy`, `Y_val.npy`, etc. A file `splits.json`, which indicates which training indexes to downsample during ensemble training, is also saved. These steps can be reproduced by running `scripts/02_construct_datasets.py`.

S1.3. Hyperparameter tuning setup

Hyperparameter tuning was performed for all possible modality combinations using Hydra’s Optuna plugin. Wrapper code in Crescendo was used to run these scripts. The following hyper-parameters were tuned in all cases:

- Neural network architecture: starting from the input size of 200, 400 or 600 input neurons (the discretized, possibly multi-modal XANES spectrum), and ending with the output size corresponding to the number of chemical motifs in that dataset (between 36 and 42), the number of hidden layers is varied. The number of neurons per layer is determined by a simple linear ramp from the input size to the output size. For example, a linear ramp of 2 hidden neurons between input size of 10 and output size of 4 would simply result in an architecture of [10, 8, 6, 4]. In these experiments, the number of hidden layers was chosen from the set {6, 9, 12, 15, 18, 21}.
- The training mini-batch size was chosen from the set {128, 256, 512, 1024}.
- The initial Adam optimizer learning rate was chosen from a continuous range (0.001, 0.01).
- The dropout rate was chosen from the continuous range (0, 0.1).

Optuna executed 100 total trials in order to determine the optimal hyper-parameter set. Hyper-parameter tuning was performed for 500 epochs, using an early stopping criterion and learning-rate-decrease-on-validation-loss-plateau scheduler. All models use batch normalization, except the last layer, and a Sigmoid output layer. The best set of hyper-parameters in each case was used as the starting point for the training of the neural network ensembles.

S1.4. Neural network ensemble details

Starting from the hyper-parameters found in the previous section, a set of 20 estimators is each trained for at most 1000 epochs using the same criteria as in the hyper-parameter tuning. Each estimator has a randomized architecture, which is constructed by starting from the scaffold found in the hyper-parameter search, and randomly distorting each layer by rounded Gaussian noise with standard deviation 10. Further model diversity was created by a random down-sampling of the training sets, such that each estimator is trained on a different 95% sampling of the full training set.

S1.5. Evaluation details

Each individual model, whether part of an ensemble or not, is treated as its own *classifier*. Thus, for a single estimator, its prediction is the binary vector corresponding to the rounded neural network output. In an ensemble, the prediction is the rounded mean of these binary vectors. The number of deviating estimators is of course the number of estimators that disagree with the majority opinion, as outlined in the main text.

S2. SUPPLEMENTAL FIGURES AND TABLES

In this section, we present supplemental figures and tables to add additional context to the content presented in the main text.

First, we showcase a demonstration of the multimodal advantage when using *pairs* of modalities (as opposed to all of the modalities as in the main text). The objective of this analysis is to confirm that pairs of modalities also provide an advantage over single modalities in most cases. These results are presented in Fig. S1. Indeed, it is the case that the CBA score on average for double-modality models is higher than the corresponding single modalities. There are cases in which this is not the case (e.g. alkenes and the N- and O-containing spectra), but these correspond to situations where the XANES signal should not be assumed to contain the relevant information required to make the predictions.

Next, in Fig. S2, we show the UQ results of the 8/9 split dataset. This dataset used only molecules with up to and including 8 heavy atoms/molecule for training and validation, but tested on the (far larger) split of molecules containing 9 heavy atoms/molecule. While the models perform slightly worse overall, they are still quite robust and provide accurate UQ in almost all cases, mirroring the results in the main text using the random data splits.

Finally, we present some additional information on some of the commonly occurring chemical motifs in the \mathcal{D}_{CNO} dataset. Fig. S3 showcases examples of these motifs, and Tab. S1 contains additional details on each chemical motif. For further details, we refer the reader to the source of truth for the SMARTS patterns which can be found in the previously mentioned GitHub repository, github.com/openbabel/openbabel/blob/master/data/SMARTS_InteLigand.txt.

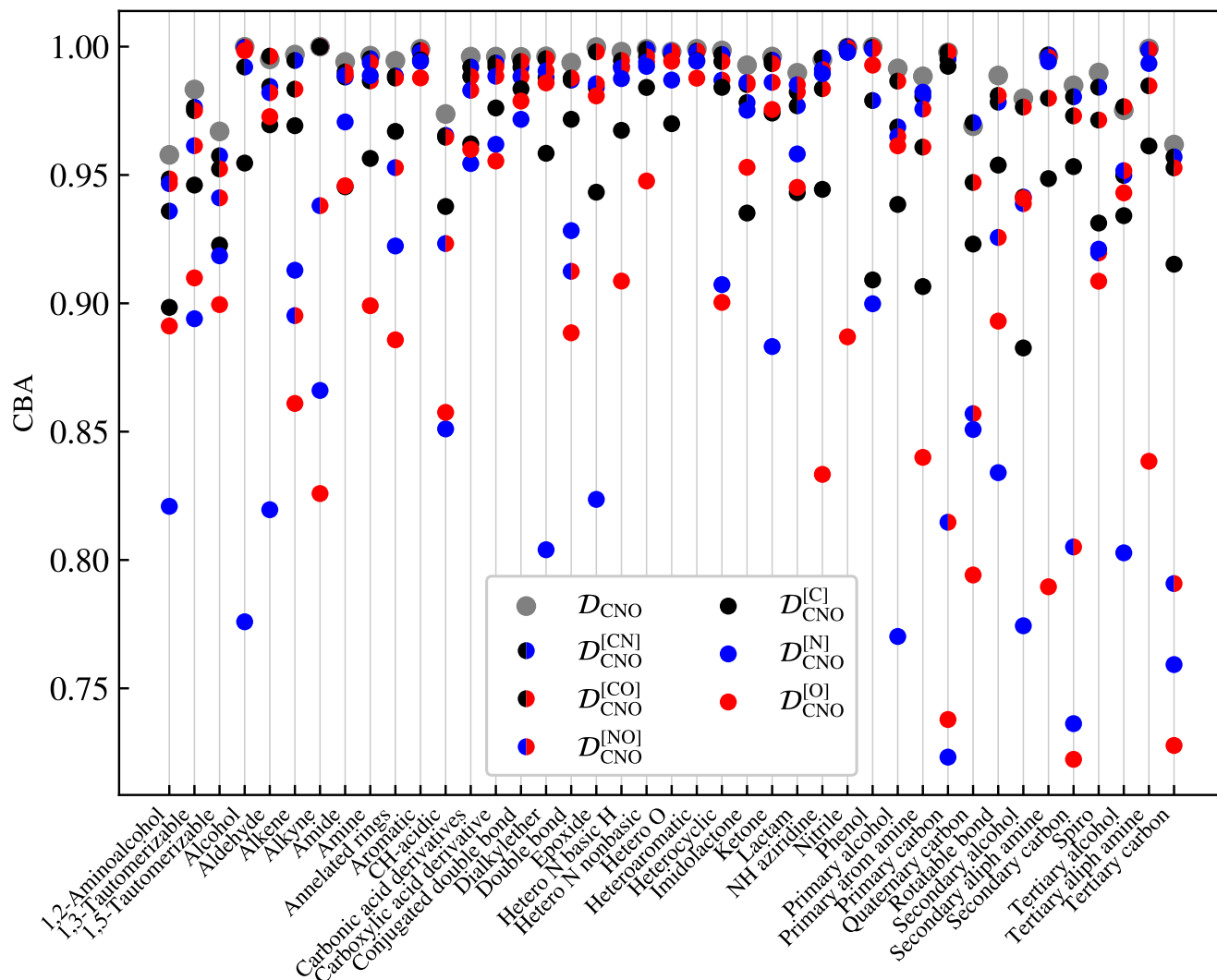


FIG. S1. Demonstration of the multimodal advantage using pairs of modalities in addition to those presented in Fig. 3.

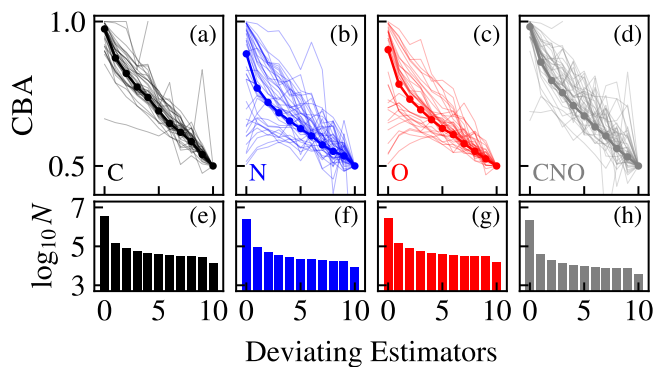


FIG. S2. Uncertainty quantification using neural network ensembles for the 8/9 split datasets. Notation is identical to Fig. 4.

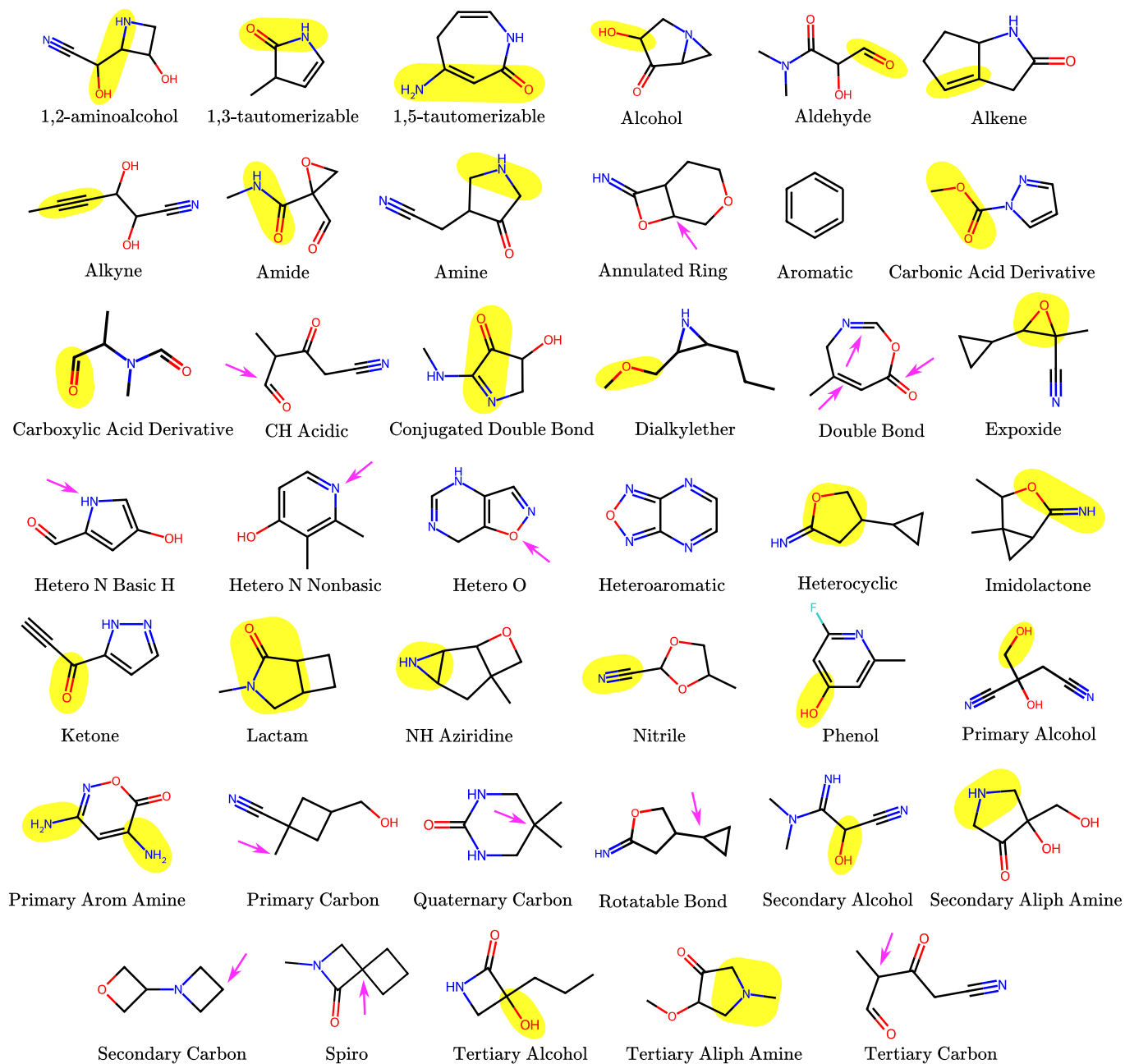


FIG. S3. Enumerated chemical motifs used in Fig. 3 of the main text. Details of each chemical motif are presented in Tab. S1.

TABLE S1. Further details on the chemical motifs. Note that some of these classifications are slight misnomers. For example, a phenol group is formally of the chemical formula C_6H_5OH , but the FP4 fingerprinting method includes alcohols bonded to *any* aromatic group. A “+” symbol is used in place of a triple bond.

Chemical Motif	Representation	Description
1,2-aminoalcohol	-	An amine and alcohol separated by two carbon atoms
1,3-tautomerizable	-	Structural isomers that interconvert at the 1 and 3 positions
1,5-tautomerizable	-	Structural isomers that interconvert at the 1 and 5 positions
Alcohol	COH	A carbon single-bonded to an oxygen atom
Aldehyde	RCH=O	A C-O double bond where C is attached to at least one H
Alkene	RR'C=CR''R'''	A C-C double bond
Alkyne	RC+CR'	A C-C triple bond
Amide	RC(=O)NR'R''	A carbon double-bonded to an oxygen and single bonded to a nitrogen
Amine	RR'R''N	A nitrogen bonded to at least one carbon chain
Annulated Ring	-	Fused rings such that more than one rings shares at least two atoms
Aromatic	-	A conjugated system containing $4n + 2$ π -electrons
Carbonic Acid Derivative	-	A molecule derived from a carbonic acid
Carboxylic Acid Derivative	-	A molecule derived from a carboxylic acid
CH Acidic	-	C-H bonded to a carbon on a carbonyl, nitro, or similar
Conjugated Double Bond	-	A double bond that is part of an extended π orbital system
Dialkylether	ROR'	An oxygen bonded to two carbon chains
Double Bond	-	A molecule containing a double bond
Epoxyde	-	An ether contained in a 3-membered ring of carbon atoms
Hetero N Basic H	-	A nitrogen contained in a ring with a basic H
Hetero N Nonbasic	-	A nitrogen contained in a ring which does not have basic character
Hetero O	-	Oxygen atom contained in a ring
Heteroaromatic	-	A non-carbon atom contained in an aromatic system
Heterocyclic	-	A non-carbon atom contained in a ring
Imidolactone	-	A carbon atom double-bonded to a nitrogen and single-bonded to an oxygen
Ketone	R(C=O)R'	A carbon atom double bonded to an oxygen and two carbon chains
Lactam	-	A cyclic amide
NH Aziridine	-	An amide contained in a 3-membered ring of carbon atoms
Nitrile	RC+N	A C-N triple bond
Phenol	-	An alcohol connected to an aromatic ring
Primary Alcohol	RCH ₂ OH	An alcohol in which the base carbon is bonded to two hydrogen atoms
Primary Arom Amine	-	An amine group connected to an aromatic ring
Primary Carbon	RCH ₃	A carbon atom bonded to three hydrogen atoms
Quaternary Carbon	RR'R''R'''C	A carbon atom bonded to four carbon atoms
Rotatable Bond	-	A rotatable bond of σ character
Secondary Alcohol	RR'CHOH	An alcohol in which the base carbon is bonded to one hydrogen atom
Secondary Aliph Amine	RR'NH	An amine bonded to two carbon groups
Secondary Carbon	RR'CH	A carbon atom bonded to two carbon atoms
Spiro	-	Two rings that share a single atom
Tertiary Alcohol	RR'R''COH	An alcohol in which the base carbon is bonded to three carbon atoms
Tertiary Aliph Amine	RR'R''N	An amine bonded to three carbon groups
Tertiary Carbon	RR'R''C	A carbon atom bonded to three carbon atoms

-
- [1] G. Carleo and M. Troyer, Solving the quantum many-body problem with artificial neural networks, *Science* **355**, 602 (2017).
 - [2] Y. Nomura, A. S. Darmawan, Y. Yamaji, and M. Imada, Restricted boltzmann machine learning for solving strongly correlated quantum systems, *Phys. Rev. B* **96**, 205152 (2017).
 - [3] Z. Cai and J. Liu, Approximating quantum many-body wave functions using artificial neural networks, *Physical Review B* **97**, 035116 (2018).
 - [4] E. J. Sturm, M. R. Carbone, D. Lu, A. Weichselbaum, and R. M. Konik, Predicting impurity spectral functions using machine learning, *Phys. Rev. B* **103**, 245118 (2021).
 - [5] C. Miles, M. R. Carbone, E. J. Sturm, D. Lu, A. Weichselbaum, K. Barros, and R. M. Konik, Machine learning of kondo physics using variational autoencoders and symbolic regression, *Phys. Rev. B* **104**, 235111 (2021).
 - [6] J. Lee, M. R. Carbone, and W. Yin, Machine-learning the spectral function of a hole in a quantum antiferromagnet, arXiv preprint [arXiv:2301.07906](https://arxiv.org/abs/2301.07906) (2023).
 - [7] J. Behler and M. Parrinello, Generalized neural-network representation of high-dimensional potential-energy surfaces, *Phys. Rev. Lett.* **98**, 146401 (2007).
 - [8] R. Gómez-Bombarelli, J. N. Wei, D. Duvenaud, J. M. Hernández-Lobato, B. Sánchez-Lengeling, D. Sheberla, J. Aguilera-Iparraguirre, T. D. Hirzel, R. P. Adams, and A. Aspuru-Guzik, Automatic chemical design using a data-driven continuous representation of molecules, *ACS Cent. Sci.* **4**, 268 (2018).
 - [9] B. Burger, P. M. Maffettone, V. V. Gusev, C. M. Aitchison, Y. Bai, X. Wang, X. Li, B. M. Alston, B. Li, R. Clowes, *et al.*, A mobile robotic chemist, *Nature* **583**, 237 (2020).
 - [10] J. Jumper, R. Evans, A. Pritzel, T. Green, M. Figurnov, O. Ronneberger, K. Tunyasuvunakool, R. Bates, A. Židek, A. Potapenko, *et al.*, Highly accurate protein structure prediction with alphafold, *Nature* **596**, 583 (2021).
 - [11] M. R. Carbone, S. Yoo, M. Topsakal, and D. Lu, Classification of local chemical environments from x-ray absorption spectra using supervised machine learning, *Phys. Rev. Mater.* **3**, 033604 (2019).
 - [12] S. B. Torrisi, M. R. Carbone, B. A. Rohr, J. H. Montoya, Y. Ha, J. Yano, S. K. Suram, and L. Hung, Random forest machine learning models for interpretable x-ray absorption near-edge structure spectrum-property relationships, *npj Comput. Mater.* **6**, 1 (2020).
 - [13] C. D. Rankine and T. Penfold, Accurate, affordable, and generalizable machine learning simulations of transition metal x-ray absorption spectra using the xanesnet deep neural network, *J. Chem. Phys.* **156**, 164102 (2022).
 - [14] T. Penfold and C. Rankine, A deep neural network for valence-to-core x-ray emission spectroscopy, *Molecular Physics* , e2123406 (2022).
 - [15] A. Lavecchia, Machine-learning approaches in drug discovery: methods and applications, *Drug discovery today* **20**, 318 (2015).
 - [16] J. Vamathevan, D. Clark, P. Czodrowski, I. Dunham, E. Ferran, G. Lee, B. Li, A. Madabhushi, P. Shah, M. Spitzer, *et al.*, Applications of machine learning in drug discovery and development, *Nature reviews Drug discovery* **18**, 463 (2019).
 - [17] R. W. Epps, M. S. Bowen, A. A. Volk, K. Abdel-Latif, S. Han, K. G. Reyes, A. Amassian, and M. Abolhasani, Artificial chemist: an autonomous quantum dot synthesis bot, *Adv. Mater.* **32**, 2001626 (2020).
 - [18] E. Stach, B. DeCost, A. G. Kusne, J. Hattrick-Simpers, K. A. Brown, K. G. Reyes, J. Schrier, S. Billinge, T. Buonassisi, I. Foster, *et al.*, Autonomous experimentation systems for materials development: A community perspective, *Matter* **4**, 2702 (2021).
 - [19] P. M. Maffettone, A. C. Daly, and D. Olds, Constrained non-negative matrix factorization enabling real-time insights of in situ and high-throughput experiments, *Applied Physics Reviews* **8**, 041410 (2021).
 - [20] P. M. Maffettone, J. K. Lynch, T. A. Caswell, C. E. Cook, S. I. Campbell, and D. Olds, Gaming the beamlines—employing reinforcement learning to maximize scientific outcomes at large-scale user facilities, *Machine Learning: Science and Technology* **2**, 025025 (2021).
 - [21] T. Konstantinova, P. M. Maffettone, B. Ravel, S. I. Campbell, A. M. Barbour, and D. Olds, Machine learning enabling high-throughput and remote operations at large-scale user facilities, *Digital Discovery* **1**, 413 (2022).
 - [22] P. M. Maffettone, D. B. Allan, S. I. Campbell, M. R. Carbone, T. A. Caswell, B. L. DeCost, D. Gavrilov, M. D. Hanwell, H. Joess, J. Lynch, *et al.*, Self-driving multimodal studies at user facilities, arXiv preprint [arXiv:2301.09177](https://arxiv.org/abs/2301.09177) (2023).
 - [23] K. T. Butler, D. W. Davies, H. Cartwright, O. Isayev, and A. Walsh, Machine learning for molecular and materials science, *Nature* **559**, 547 (2018).
 - [24] J. Timoshenko, D. Lu, Y. Lin, and A. I. Frenkel, Supervised machine-learning-based determination of three-dimensional structure of metallic nanoparticles, *The Journal of Physical Chemistry Letters* **8**, 5091 (2017), PMID: 28960990.
 - [25] P. K. Routh, Y. Liu, N. Marcella, B. Kozinsky, and A. I. Frenkel, Latent representation learning for structural characterization of catalysts, *The Journal of Physical Chemistry Letters* **12**, 2086 (2021).
 - [26] Z. Liang, M. R. Carbone, W. Chen, F. Meng, E. Stavitski, D. Lu, M. S. Hybertsen, and X. Qu, Decoding structure-spectrum relationships with physically organized latent spaces, *Physical Review Materials* **7**, 053802 (2023).
 - [27] Y. Liu, A. Halder, S. Seifert, N. Marcella, S. Vajda, and A. I. Frenkel, Probing active sites in cu x pd y cluster catalysts by machine-learning-assisted x-ray absorption spectroscopy, *ACS Applied Materials & Interfaces* **13**, 53363 (2021).
 - [28] C. Zheng, C. Chen, Y. Chen, and S. P. Ong, Random forest models for accurate identification of coordination environments from x-ray absorption near-edge structure, *Patterns* **1**, 100013 (2020).
 - [29] A. Aarva, V. L. Deringer, S. Sainio, T. Laurila, and M. A. Caro, Understanding x-ray spectroscopy of carbonaceous ma-

- terials by combining experiments, density functional theory, and machine learning. part i: Fingerprint spectra, *Chemistry of Materials* **31**, 9243 (2019).
- [30] A. Aarva, V. L. Deringer, S. Sainio, T. Laurila, and M. A. Caro, Understanding x-ray spectroscopy of carbonaceous materials by combining experiments, density functional theory, and machine learning. part ii: Quantitative fitting of spectra, *Chemistry of Materials* **31**, 9256 (2019).
- [31] M. R. Carbone, M. Topsakal, D. Lu, and S. Yoo, Machine-learning x-ray absorption spectra to quantitative accuracy, *Phys. Rev. Lett.* **124**, 156401 (2020).
- [32] S. Tetef, N. Govind, and G. T. Seidler, Unsupervised machine learning for unbiased chemical classification in x-ray absorption spectroscopy and x-ray emission spectroscopy, *Physical Chemistry Chemical Physics* **23**, 23586 (2021).
- [33] S. Tetef, V. Kashyap, W. M. Holden, A. Velian, N. Govind, and G. T. Seidler, Informed chemical classification of organophosphorus compounds via unsupervised machine learning of x-ray absorption spectroscopy and x-ray emission spectroscopy, *The Journal of Physical Chemistry A* **126**, 4862 (2022).
- [34] S. C. Myneni, Soft x-ray spectroscopy and spectromicroscopy studies of organic molecules in the environment, *Reviews in Mineralogy and Geochemistry* **49**, 485 (2002).
- [35] C. K. Boyce, G. D. Cody, M. Feser, C. Jacobsen, A. H. Knoll, and S. Wirick, Organic chemical differentiation within fossil plant cell walls detected with x-ray spectromicroscopy, *Geology* **30**, 1039 (2002).
- [36] G. Cody, R. Botto, H. Ade, and S. Wirick, The application of soft x-ray microscopy to the in-situ analysis of sporinite in coal, *International Journal of Coal Geology* **32**, 69 (1996).
- [37] M. Uesugi, H. Naraoka, M. Ito, H. Yabuta, F. Kitajima, Y. Takano, H. Mita, I. Ohnishi, Y. Kebukawa, T. Yada, *et al.*, Sequential analysis of carbonaceous materials in hayabusa-returned samples for the determination of their origin, *Earth, Planets and Space* **66**, 1 (2014).
- [38] J. J. Rehr, J. J. Kas, F. D. Vila, M. P. Prange, and K. Jorissen, Parameter-free calculations of x-ray spectra with feff9, *Phys. Chem. Chem. Phys.* **12**, 5503 (2010).
- [39] R. Ramakrishnan, P. O. Dral, M. Rupp, and O. A. Von Lilienfeld, Quantum chemistry structures and properties of 134 kilo molecules, *Sci. Data* **1**, 1 (2014).
- [40] L. Ruddigkeit, R. Van Deursen, L. C. Blum, and J.-L. Reymond, Enumeration of 166 billion organic small molecules in the chemical universe database gdb-17, *J. Chem. Inf. Model* **52**, 2864 (2012).
- [41] A. Ghose, M. Segal, F. Meng, Z. Liang, M. S. Hybertsen, X. Qu, E. Stavitski, S. Yoo, D. Lu, and M. R. Carbone, Uncertainty-aware predictions of molecular x-ray absorption spectra using neural network ensembles, *Physical Review Research* **5**, 013180 (2023).
- [42] M. R. Carbone and D. Lu, Database of small molecule X-ray absorption spectra, featurized structures, and neural network ensembles, [10.5281/zenodo.7554888](https://doi.org/10.5281/zenodo.7554888) (2023).
- [43] G. D. Cody, H. Ade, M. O. Alexander, T. Araki, A. Butterworth, H. Fleckenstein, G. Flynn, M. K. Gilles, C. Jacobsen, A. Kilcoyne, *et al.*, Quantitative organic and light-element analysis of comet 81p/wild 2 particles using c-, n-, and o- μ -xanes, *Meteoritics & Planetary Science* **43**, 353 (2008).
- [44] S. Urquhart and H. Ade, Trends in the carbonyl core (c 1s, o 1s) \rightarrow π^* c= o transition in the near-edge x-ray absorption fine structure spectra of organic molecules, *The Journal of Physical Chemistry B* **106**, 8531 (2002).
- [45] J. Stöhr, *NEXAFS spectroscopy*, Vol. 25 (Springer Science & Business Media, 2013).
- [46] N. M. O’Boyle, M. Banck, C. A. James, C. Morley, T. Vandermeersch, and G. R. Hutchison, Open babel: An open chemical toolbox, *Journal of cheminformatics* **3**, 1 (2011).
- [47] T. Akiba, S. Sano, T. Yanase, T. Ohta, and M. Koyama, Optuna: A next-generation hyperparameter optimization framework, in *Proceedings of the 25th ACM SIGKDD international conference on knowledge discovery & data mining* (2019) pp. 2623–2631.
- [48] M. R. Carbone, When not to use machine learning: A perspective on potential and limitations, *MRS Bulletin* **47**, 968–974 (2022).
- [49] B. Settles, *Active learning literature survey* (Computer Science Technical Report 1648, University of Wisconsin-Madison Department of Computer Sciences, 2009).